Check for updates

Three-Dimensional Analysis of Porosity in As-Manufactured Glass Fiber/Vinyl Ester Filament Winded Composites Using X-Ray Micro-Computed Tomography

Chaman Srivastava[1] · Pietro Agostino[2] · Antonios G. Stamopoulos[2] · Ben Alcock[3] · Are Strandlie[1] · Sotirios Grammatikos[1]

© The Author(s) 2023

Abstract

Filament winding is a technique to manufacture tubular composite structures and, therefore, is among the most appealing techniques for fabricating critical structures such as hollow tubes. Despite the recent advances, these structures are prone to a varying degree of porosity that may affect their mechanical performance. Therefore, the accurate detection and quantification of the manufacturing porosity is crucial. Micro-CT is most suitable for performing this activity at various scales. This work employs micro-CT for studying porosity inside an as-manufactured filament-winded composite structure. Void characteristics like volume, orientation, size, and relative volume fraction inside the hoop and helical layers are quantified inside a representative curved panel extracted from a glass fiber-vinyl ester tubular composite structure, which has not been studied in detail previously. It was observed that most voids are present in the matrix region. The voids are elliptical rod-like and spherical, with the latter present in the helical layers, which also host the majority of voids and the highest void volume fractions. The voids are highly aligned along the fiber orientation direction with higher misorientations for helical layers than the hoop layer. Large voids in base layers were created due to gaps formed during the winding process. Hence, the main goal of this study is to measure the voids' characteristics and the volumetric fraction during the stacking of filament wound hoop and helical layers during a generic filament winding pattern. The data can be further exploited as input for modeling filament winded composites in the presence of voids by researchers.

✉ Chaman Srivastava
chaman.srivastava@ntnu.no

1   ASEMlab – Laboratory for Advanced and Sustainable Engineering Materials Research, Group of Sustainable Composites, Department of Manufacturing and Civil Engineering, Norwegian University of Science and Technology, 2815 Gjøvik, Norway

2   Department of Industrial and Information Engineering and Economy (DIIIE), University of L'Aquila, Via Giovanni Gronchi, 18, 67100 Nucleo Industriale Pile L'Aquila, Italy

3   Department of Materials and Nanotechnology, SINTEF Industry, 0373 Oslo, Norway

 Springer

1 Introduction

Due to the ever-increasing need for lightweight structures in civil applications [1], filament-winded polymer composite materials are increasingly employed. This is due to their increased specific properties like stiffness. Thus composites can be used in various sectors, like aeronautics, automotive, marine, renewable energy, etc. To reduce manufacturing costs, automation plays a significant role. As such, filament winding is a process that has received considerable attention due to its increased versatility, continuous production, and high throughput [2], enabling its use for tubular geometries, which can be employed in sectors like gas storage [3], wind energy [4], oil transport from offshore wells [5, 6] and electrical insulation [7]. Filament winding involves an automated procedure for laying up unidirectional tapes or pre-impregnated fiber tows around a cylindrical mandrel in a specific filament winding pattern. The technique allows continuous fiber reinforcements, offering the advantage of producing tailored filament orientation with constant or variable winding angles. This orientation is selected to match the magnitude of the stresses expected to be developed within the bulk of the filament-winded structure while in use. The process hence can easily be robotized [8], reducing labor costs and related manufacturing waste [9].

Various manufacturing parameters can affect the properties of filament-winded polymer composite, such as deviation from the predefined winding angle [10, 11], which can degrade the overall performance of a tubular structure [11]. Another parameter that has been taken into consideration in the works of Lisboa et al. [12], Dalibor et al. [13], and Rousseau et al. [14] is the pattern created, even when the winding angle is constant, on helicoidally winded tubes. Nevertheless, a typical result of any filament winding process is the creation of voids, which can vary in shape, size, location, and spatial orientation depending on the processing and post-processing employed. Voids and hence porosity are always present, in filament-winded composites, without implications on the final quality. In general terms, porosity might affect composite materials' matrix-dominated properties [15–17], and its presence is directly related to the quality of the manufacturing process [18]. The filament winding process is thus promising, because of the tension applied to filaments causes the tows compaction which, tends to increase quality [19] but on contrary can also lead to squeezing of matrix as explained further.

During the filament winding fabrication process, predefined winding tension is applied for the compaction of the fiber bed and for making the final part denser as the number of layers increases. As the winding process continues, a temperature gradient is formed across the thickness of the composite structure, affecting the resin flow properties and the extent of curing [20], which may lead to the creation of voids [21]. It has been observed that the production of pores/voids during filament winding is a diffusion-related process. Voids typically grow along the fiber direction due to winding tension that squeezes the resin out. The combination of tension and elevated temperature levels leads to entrapped water vapor, creating voids [22, 23]. This phenomenon is often called the 'squeezed sponge model' [24, 25]. In some cases, if the winding of filaments does not lead to adequate consolidation, it may result in a higher void fraction [17]. This can lead to variations in the mechanical performances [26] observed.

Considering the above, accurate detection and quantification of the process-induced voids are worth investigating. The intention is to enhance the understanding of the inherent status of the structure, which will allow improvement of the structure's design, processing, and service life as a function of load-defect interactions. To this end, X-Ray Computed Tomography (micro-CT) is among the most promising Non-Destructive

Testing (NDT) methods for performing volumetric inspection of high resolution, down to the nanoscale [27]. The popularity of micro-CT in materials engineering has increased due to significant gains in spatial resolution due to rapid development in X-ray tubes and detectors [28]. Therefore, the imaging technique has been used for morphological analysis in various applications like nuclear [29], biomedical [30, 31], food engineering [32] and as input for finite element modeling of structures [17, 33]. The technique involves acquiring a series of projections (images) and combining them to create a 3D rendering of the scanned object. A greyscale intensity histogram represents the scanned object. The histogram is a function of the difference in an object's materials' absorption and scattered coefficients. The individual materials can be segmented based on the difference in the material contrast caused by differences in density. As an NDT tool, micro-CT is a reliable method for assessing the presence of porosity from micro to macro levels [34], whereas, in the case of filament-winded structures, micro-CT has shown great potential for quantifying voids and pores [35]. Slight positive correlation between the scan resolution and voxel size for the detection of voids inside composite materials has been presented by [34, 36–38] . Considerable research has been conducted in two main directions: i) automation in scanning and ii) image processing [26]. This has led micro-CT to become a robust NDT tool for detecting voids at different scales compared to other methods like optical microscopy, which are prone to section bias and a higher location-bias error [39, 40].

The rationale of this study is to understand and investigate: 1) the characteristics of porosity within composite coupons from a filament winded composite panel made from viz: hoop layer and helical layers, and 2) the variation of porosity within the structure can help create knockdown factors dependent on the volume fraction, orientation and shape of porosity within each layer [33, 41]. These knockdown factors could potentially be employed to analyze the properties of composite laminates in the presence of pores. To this end, Finite Element Analysis (FEA) can be used better to understand the global deformation and failure of filament-winded structures in the presence of voids

The work presents a three-dimensional (3D) analysis of manufacturing-induced voids within filament-winded composite panels using X-ray micro-CT. Coupons were selected along the direction of filament winding from a representative curved panel. The composite layers are laminated with different degrees of tension and orientation during a continuous process, which causes slippage, imperfect compaction, and unstable tow width that leads to gaps that may develop into voids after resin impregnation and curing. The detected voids were analyzed using the VGStudio MAX 3.4.5 industrial software to obtain void characteristics such as void morphology, void spatial location, and void volume. Further processing was conducted using inertia tensors in MATLAB 2021.2 to calculate the three orthogonal axes, providing insight into the void size and orientations. The variation in the void volume fraction within the composite panel is also presented. Interestingly, the analysis results revealed a significant variation of void and porosity characteristics across the length, thickness, and the different layers within the coupons of the extracted panel. It has been observed that helical layers, which are laminated at higher angles, tend to have higher volume fractions and spherical voids and the lowest amount of void-fiber misorientations. This critical information can be utilized (1) when selecting samples for mechanical testing of filament wound composite coupons (2) creating high fidelity models of filament wound composite laminates and structure at meso-macro scales keeping in-mind the effect voids can have towards mechanical property degradtion. For clarity purposes, where 'porosity' is mentioned, the authors refer to the 'collection of voids'.

2 Materials and Processes

To create the cylindrical pipe structure, the basic designs of filament winding are used [26], where the filaments are over-wrapped in a specific winding and stacking sequence. Helical winding (H2, ±15°) produces the base layer, followed by a second helical winding (H1, ±75°). The hoop layer (Hp) is circumferentially wrapped all along the length of the composite pipe. The winding is performed by leading dry fibers into a resin bath before the winding process. After the manufacturing procedure, the composite structure is allowed to cure at room temperature. The fiber volume fraction in the panel was calculated to be 69.4 ± 3.3%. Specimen size and scan resolution are inversely related; hence for a higher resolution, the cylindrical pipe structure is divided into 24 axial panels, such that the fiber tows are symmetrically oriented, making each panel a representative volume element. One such axial panel is shown in green in Fig. 1. The dimensions of the extracted panel are 180 × 40 × 5 mm. The liner was not removed from the composite panel before the scan to avoid creating open voids that were not detected, hence not changing the total volume fraction. The whole panel is also scanned under micro-CT to pinpoint macro-void distribution.

The extracted panel from the tubular section is further segmented into eight smaller coupons, labeled S1 to S8, using a wet-cutting machine. The coupons S1 to S8 follow the filament-winding direction from top to bottom. Hence, each coupon (S1→S8) has a different fiber orientation and volume fraction of fiber and pores. The size of each coupon is 40 × 25 × 5 mm. Representative coupons are extracted from a curved panel of a glass fiber/vinyl-ester filament winded cylindrical pipe to characterize the variation in micro and macro-porosity morphology, size, and misorientation with the nominal fiber direction. Each coupon was re-scanned to increase the overall resolution and obtain a better greyscale distribution of matrix, pores, and fiber.
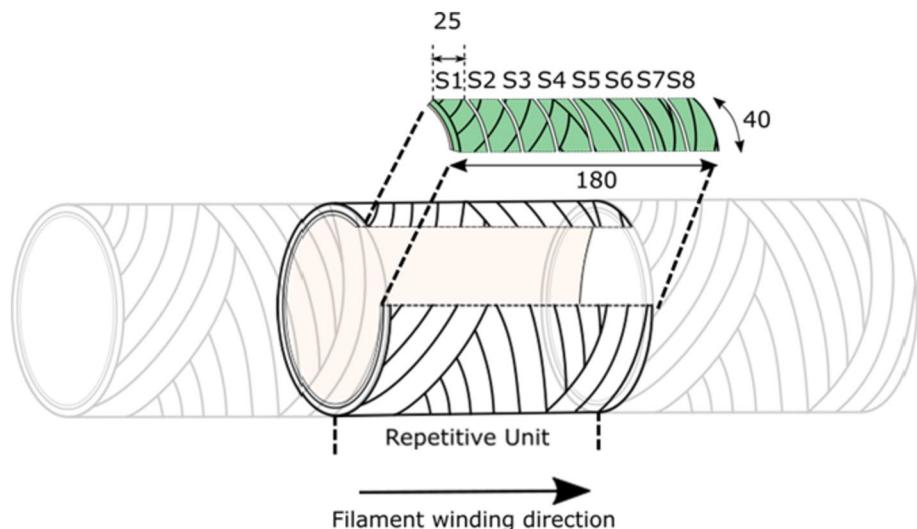

Fig. 1 A schematic representation of the dimension of the curved composite structure, (in green): 1/24th axial panel representative unit panel from tubular structure and the specimen arrangement from S1 to S8 that were analysed under micro-CT. The dimensions are in mm

2.1 X-Ray Computed Tomography: Image Acquisition, Segmentation and Analysis

The specimens obtained from the panel are mounted on the sample holder individually with the help of soft polystyrene foam and centered between the source and detector panel, as shown in Fig. 2. The scans were performed on a ZEISS Metrotom 1500 G2 Industrial CT at the Department of Manufacturing and Civil Engineering (IVB) of NTNU Gjøvik. The detector panel size is 2048 × 2048 pixels and has a detectable theoretical resolution of 8 μm with a maximum of 6000 projections through the specimen. The attenuation of the X-rays due to the material density and geometry is used as a measuring principle, and the volumetric data is generated using the Feldkamp reconstruction algorithm. The tube voltage and current are set to 100 kV and 250 μA for scanning the specimens, respectively. The specimens are scanned using the 'stop-and-go' method, where the specimens are rotated 0.17°/s with an integration time of 1s. The total number of projections through the scanned specimens was set to 2050. This was done to make a balance between the optimum resolution and the size of the dataset. The average time for each scan was approximately 80 mins. In addition, the specimen is kept closer to the X-Ray source to achieve higher resolution. The overall resolution defined by the voxel size in the x-y-z direction was 26 μm, with approximately 1.7 Bn voxels on each scanned composite coupon.

The reconstructed 3D scans were processed in an industrial CT software –VGStudio MAX from Volume Graphics (Heidelberg, Germany), also known from previous works in this field [41]. The segmentation of the voids from the composite material was done in 2 stages. Firstly, a Region of Interest (ROI) is created, chamfering the rough edges from the cutting process, followed by a surface determination based on the intensity of the grey value. Hence, a curved cuboidal section contains reinforcing fibers, polymers and voids.

Regarding the segmentation process, a surface determination is carried out based on the grey value, which separates the background and voids from the bulk of the composite material. To accommodate the partial volume effect, an automatic grey value threshold, implemented in software based on the ISO50 threshold [29, 30], was a reliable choice regarding accuracy in
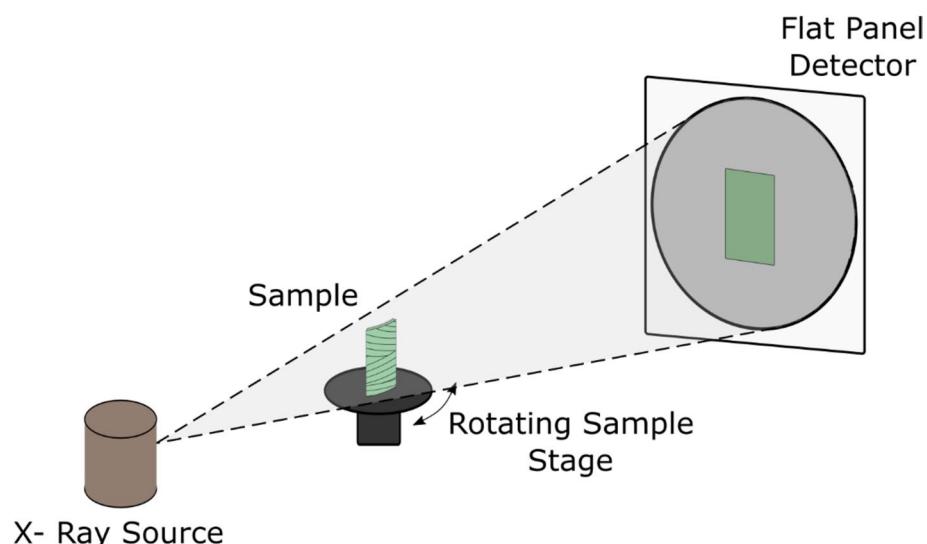

Fig. 2 Micro-CT setup for scanning composite coupons

segmenting individual components of the composite material. Another ROI analysis was conducted to discretise each curved cuboidal composite coupon into hoop layer (referred as [Hp]) , middle helical layers (referred to as [H1]), and the base helical layer (referred to as [H2]), which make the middle and bottom laminate respectively. A porosity detection algorithm was utilized to quantify the voids, incorporating segmentation, a grey value threshold, and a probability criterion, which is optimum for segregating pores from the bulk of the material [22]. As reported in previous works [40, 42, 43], accurately defining the threshold for a given voxel size and a predefined attenuation coefficient of the materials involved in the micro-CT scanning is fundamental for accurately identifying the pores. Micro-porosity is filtered out by setting the minimum detectable volume to 0.0046 mm^3 (0.026^3× 263 voxels). At the same time, a probability threshold is imposed, related to a probability algorithm regarding the grey scale values of the detected pores, as also seen by Stamopoulos et al. [41]. Hence, the differentiation is based on two criteria: 1) the probability criterion of the grey scale value and 2) the volume of the pores. Figure 3 presents the grey value rendering and the detected voids in Specimen 1 (S1). The characteristics dataset consists of volumes, morphology, and the centroid of each void, where the latter defines the 3-dimensional location of each void inside the composite coupon. The sphericity of the voids (ψ) is calculated using Eq. 1.

$$\langle \psi \rangle = \frac{A_{sphere}}{A_{void}} \tag{1}$$

where A_{sphere} and A_{void} are the surface area of the sphere fitted to voids and the surface area of the voids, respectively. The elongation *(el)* and the flatness *(fl)* of the voids are measured using Eqs. 2 and 3. The size of the voids is calculated by fitting an ellipsoid having the same inertia tensor to the voids'. The ellipsoids' three orthogonal semi-axes are calculated using a Principal Component Analysis (PCA). The elongation and flatness of voids are calculated by the formulation provided by Zingg [44].

$$el = \frac{b_2}{b_1} \tag{2}$$
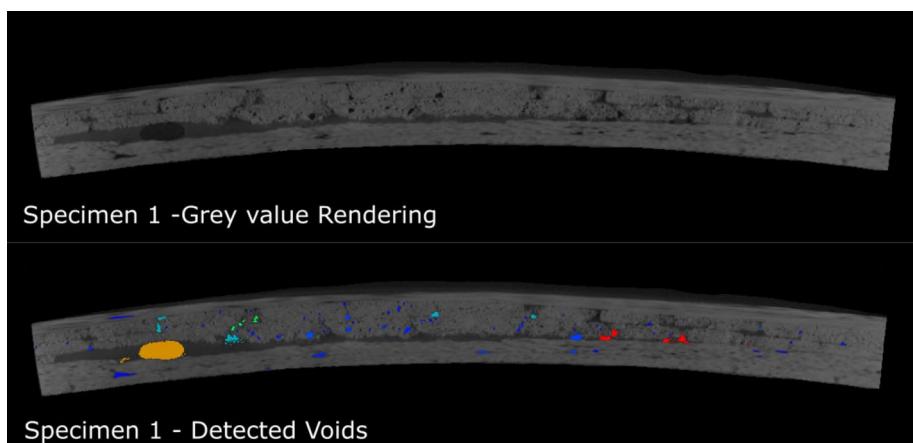
Fig. 3 Grey value rendering of scanned composite coupon (S1) as-original (top) detected meso-macro voids colour coded as per the volume of voids (bottom)

$$fl = \frac{b_3}{b_2} \tag{3}$$

where b_1, b_2, and b_3 are the semi-major, semi-medium and semi-minor axes of the closest fitting ellipse to the voids. The dataset's statistical analysis and visual 3D representations were obtained using Python and VGStudio MAX.

3 Results and Discussion

The results of the micro-CT analysis of the coupons from S1 to S8, taken from the filament-winded composite panel along the winding direction, are presented in this section. The tomographic sliced section of a representative coupon is presented in Fig. 3. It can be observed that the voids, vinyl-ester matrix, and glass fiber have a varied distribution of greyscale intensity, and the voids appear as dark black spots inside the material, which are then detected and can be color-coded based on measurements like the volume of the voids. As the slices are 2D images, getting an overview of the void morphology and size is complex as the voids usually extend along the direction of the filament winding and can have different cross-sectional geometry, as visible in Fig. 3. Thus, a section-bias error is created, making micro-CT a superior choice to study porosity than optical microscopy[40].

A 3D visualization of the voids in the individual hoop layer [Hp], helical layer [H1]-middle layer, and helical layer [H2] – bottom layer from specimen S1 to S8, segmented from the bulk of the composite material is presented in, Figs. 4, 5 and 6 respectively. The voids (presented in green, blue, and red, respectively) appear as both elongated and spherical features where most of the elongated features are presented between and inside the tows of the filament, and the spherical voids are mostly entrapped between the bulk vinyl ester matrix. The hoop layer primarily consists of long and thin elongated pores, mostly intra-filament positioned, while the larger pores are placed between consecutive filaments. Besides the low sphericity and elongated pores, high sphericity pores in the specimen's resin-rich areas favor their presence, mainly in the middle helical layer [H1].

The overall voidage inside the coupons S1 to S8 (hoop and helical layers combined), as a function of the location of the coupons and along the filament winding direction, is found to have a sigmoidal behaviour, as presented in Fig. 7. It can be observed that the porosity is low volumetrically, but the number of voids is significant enough to create a reliable statistical analysis. Nevertheless, even though the voids follow this pattern, the overall content is not the same for each examined coupon. Coupons close to the central zone of the panel appear to have fewer small-sized pores and a higher quantity of larger pores. The volume fraction varies between 0.74 and 1.25 %, resulting in an average value of 0.79%. The highest value is registered for the specimen taken from the centre of the extracted [S4-S5] panel, while the minimum is at S8, located towards the end of the cylindrical panel. Large, elongated voids are observed at the bottom layer [H2].
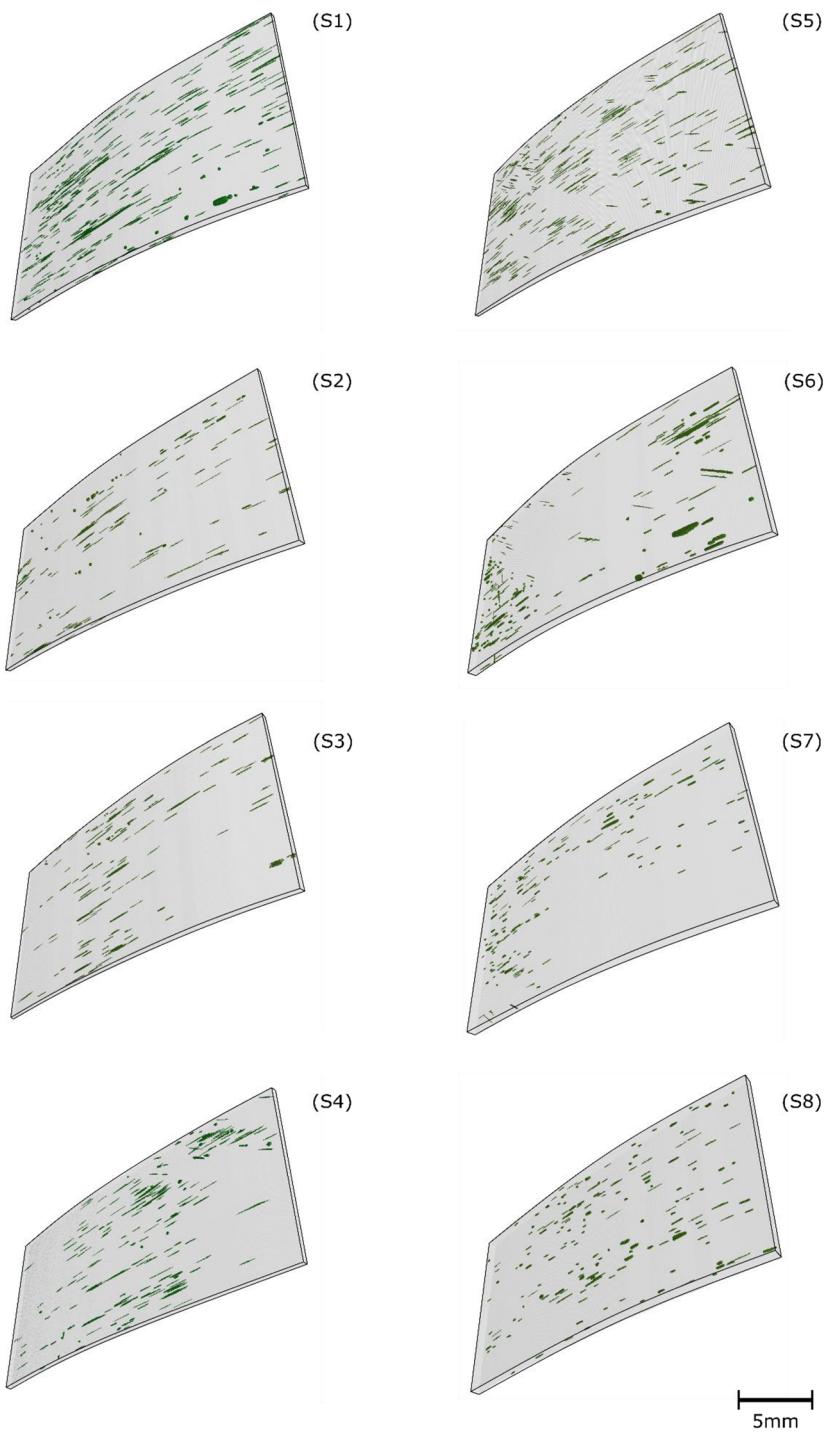
Fig. 4 3D rendering of voids from hoop layer [Hp] segmented specimen. In this figure, the fibers and matrix are transparent, while the voids are shown in green inside the bounding box
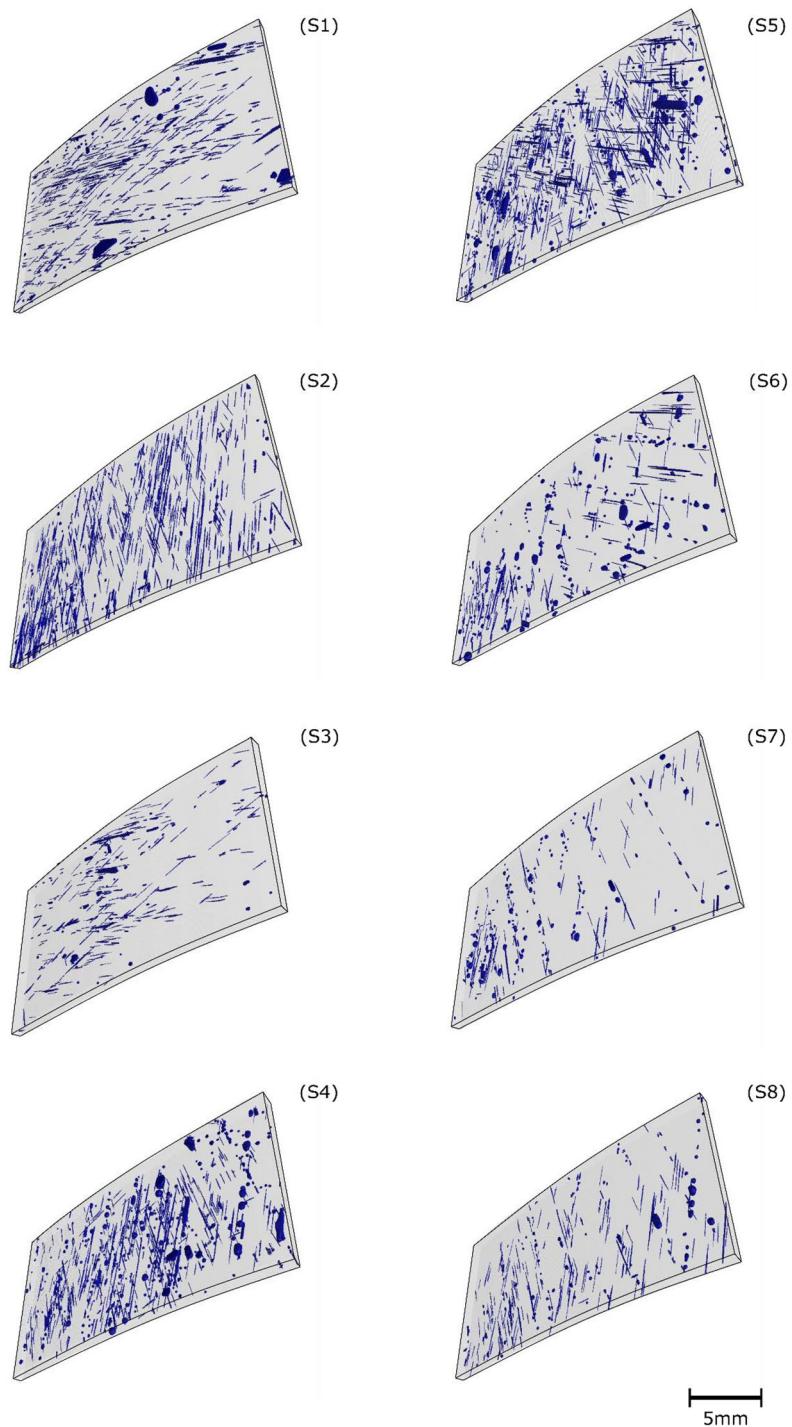
Fig. 5 3D rendering of voids from middle helical layer [H1] segmented specimen. In this figure, the fibers and matrix are transparent, while the voids are shown in blue inside the bounding box
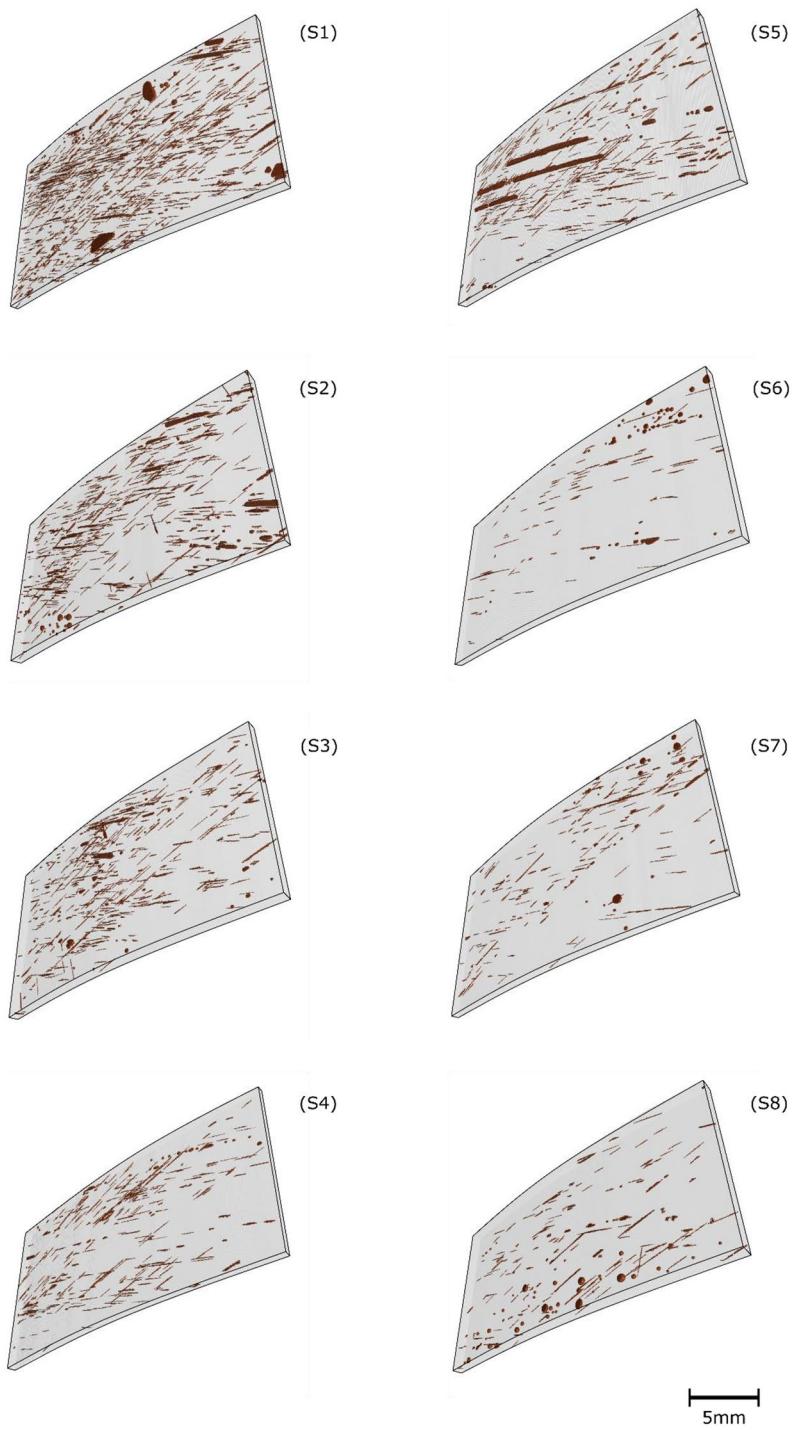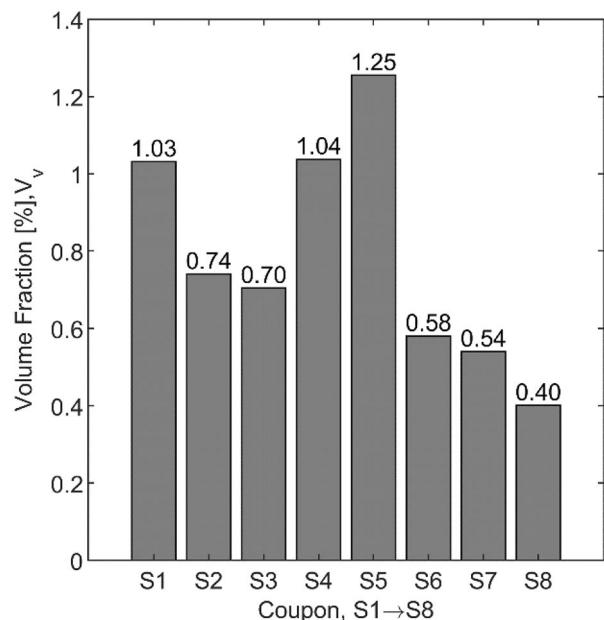
Fig. 6 3D rendering of voids from base helical layer [H2] segmented specimen. In this figure, the fibers and matrix are transparent, while the voids are shown in brown inside the bounding box

3.1 Analysis of Voids' Size Parameters- Major, Medium and Minor Axes

The three components of the principal component analysis (PCA) and the corresponding eigenvalues from ellipsoidal fitting to the voids were used to calculate the three size geometrical parameters of voids detected inside the filament winded composite coupons. As the laminate has a curved geometry, a cartesian coordinate system was created where the origin for measurement of the ellipsoidal centroid was offset by the radius (R) of the cylinder fitted to the curved geometry. Thus, the location of the void's centroid (R,x1,x2) is measured from the central axis of the curved panel, as presented in Fig. 8(a). An illustration of the voids fitted to an ellipsoid is presented in Fig. 8(b). The three semi-major (b_1), semi-medium (b_2) and semi-minor (b_3) axes are calculated using the computational formulation presented by Padfield and Miller [45] implemented in MATLAB 2021.2.

To better understand the variation in the sizes of each void, three different ROIs were created in each coupon, which segregates the laminates into three dominant layers (hoop and two helical layers), as described in Section 2. The distribution and comparison in the size parameters are reported for each laminate layer. The size distribution within each laminate is significant; however, a smaller range can be defined based on the global mean value for comparison with other layers. A detailed statistical data analysis for voids detected in each specimen (S1 to S8) is presented in Tables 1, 2 and 3 for the distribution of the size parameters from the hoop layer [Hp] and middle and base helical layers [H1, H2] respectively. As a general observation, it can be postulated that voids are mostly ellipsoidal with principal axes, much longer than the medium and minor axes. Smaller circular voids are also detected, and the variation in

(a) Composite Coupon (S$_i$)

Void (R,x1,x2)

x2

x1

R

Axial Panel Central Axis

(b) PCA 1

(b$_1$)

PCA 3
(b$_3$)

PCA 2 (b$_2$)

Void (R,x1,x2)
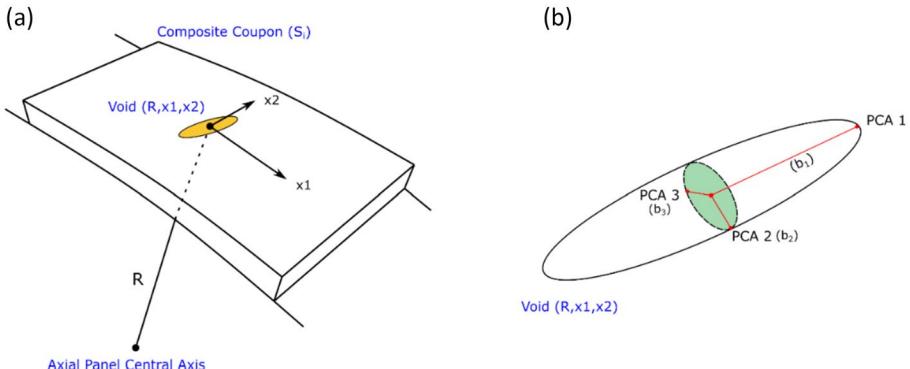
Fig. 8 **a** Cartesian coordinate system selected for position and orientation measurement **b** ellipsoidal fitting to voids with PCA vectors

their volume fraction is found to differ between the hoop and helical layers, where the latter hosts most of them.

Figure 9 presents the variation of the three orthogonal size parameters for voids detected inside each layer and of each specimen. Moving on the x' axis of the graphs of Fig. 9, from left to right, follows the filament winding direction, representing the position of each specimen. The y-axis plots the size parameters, and the concentration of the data points reflects the distribution via a strip plot. For the voids located inside the hoop layer of all the composite coupons (S1 to S8), it can be observed that the size parameters for the semi-major axis are more pronounced when compared to the semi-medium and semi-minor axes. The average and standard deviation in the semi-major, semi-medium and semi-minor axis calculated over all the specimens are 0.713 ± 0.36 mm, 0.079 ± 0.03mm and 0.051 ± 0.019mm, respectively. It is approximated that the principal axis of the voids is nearly 10 times longer when compared to the other two orthogonal axes, which are also unequal, but with a slight difference. Thus voids are hence elongated rod-like in shape with a circular cross. The average 95th percentile of the semi-major, medium and minor axes amongst the different specimens is 1.33, 0.135 and 0.092, respectively. It can be observed that a small percentage of voids also have an elliptical cross-section and are flat.

Voids detected within the middle helical layer [H1], the global average with the deviation for the three orthogonal axes of the voids is 0.802±0.60 mm, 0.092±0.05 mm and 0.061±0.03 mm. Similarly, a rod-like shape with a rather circular cross-section is predicted for voids. It is observed that the size parameters exhibit the highest values for this layer when compared to the hoop and the base helical layer. The highest scatter in the interquartile range is also observed for the middle helical layer. The global average 95th percentile of the semi-major, medium and minor axes amongst the different specimens is 1.91, 0.195 and 0.132. Minor changes are visible for a relatively small percentage of ellipsoidal voids for medium and minor axes, but the major axes are nearly 2.3 times larger than the mean void. The layers also show the highest coefficient of variation amongst the size parameters of the voids. It is also noted that intra-sample distribution in the medium and minor size parameters for the

Table 1 Statistical data for variation of semi-major axes of ellipsoidal voids detected in FW composite coupons along filament winding direction [mm]

Intra-Laminate Average (S1 to S8)

Specimen#	Specimen 1			Specimen 2			Specimen 3			Specimen 4			Specimen 5			Specimen 6			Specimen 7			Specimen 8		
Layer	Hp	H1	H2	Hp	H1	H2	Hp	H1	H2	Hp	H1	H2	Hp	H1	H2	Hp	H1	H2	Hp	H1	H2	Hp	H1	H2
Average	0.87	1.01	0.81	0.70	0.97	0.86	0.79	0.69	0.76	0.76	0.69	0.83	0.98	0.83	0.92	0.54	0.64	0.71	0.55	0.85	0.81	0.47	0.71	0.61
Std. Dev.	0.46	0.63	0.43	0.38	0.58	0.45	0.39	0.54	0.45	0.38	0.61	0.52	0.41	0.59	0.74	0.37	0.58	0.54	0.29	0.71	0.39	0.25	0.61	0.44
COV*10^{-2}	0.52	0.62	0.53	0.55	0.61	0.52	0.49	0.78	0.60	0.51	0.87	0.62	0.42	0.71	0.81	0.68	0.91	0.76	0.52	0.82	0.48	0.53	0.85	0.72
Median	0.84	0.92	0.56	0.66	0.91	0.82	0.74	0.60	0.70	0.76	0.56	0.76	0.90	0.81	0.84	0.44	0.44	0.66	0.48	0.73	0.78	0.42	0.50	0.53
95th Percentile	1.48	2.40	1.61	1.42	1.92	1.61	1.51	1.66	1.56	1.36	1.73	1.74	1.64	1.82	1.60	1.14	1.75	1.44	1.18	2.18	1.51	0.94	1.75	1.39

Global Average

Layer#	Hoop Layer [Hp]	Middle Helical Layer [H1]	Base Helical Layer [H2]
Average	0.71	0.82	0.79
Std. Dev.	0.36	0.60	0.50
COV*10^{-2}	0.52	0.77	0.63
Median	0.65	0.68	0.73
95th Percentile	1.33	1.91	1.55

Table 2 Statistical data for variation of semi-medium axes of ellipsoidal voids [mm × 10]

Intra-Laminate Average (S1 to S8)

Specimen#	Specimen 1			Specimen 2			Specimen 3			Specimen 4			Specimen 5			Specimen 6			Specimen 7			Specimen 8		
Layer	Hp	H1	H2	Hp	H1	H2	Hp	H1	H2	Hp	H1	H2	Hp	H1	H2	Hp	H1	H2	Hp	H1	H2	Hp	H1	H2
Average	0.65	0.69	0.83	0.81	0.71	0.78	0.74	1.01	0.91	0.78	1.04	0.85	0.60	0.91	0.78	1.01	1.16	1.07	0.84	0.93	0.78	0.88	0.96	1.10
Std. Dev.	0.26	0.36	0.72	0.39	0.34	0.45	0.31	0.63	0.57	0.41	0.68	0.46	0.21	0.62	0.49	0.28	0.71	0.62	0.28	0.61	0.48	0.31	0.55	0.70
COV*10^{-2}	0.40	0.51	0.87	0.49	0.48	0.58	0.40	0.63	0.62	0.51	0.65	0.53	0.38	0.69	0.63	0.28	0.62	0.58	0.33	0.65	0.62	0.34	0.57	0.63
Median	0.6	0.6	0.6	0.6	0.6	0.6	0.6	0.8	0.8	0.6	0.8	0.8	0.6	0.6	0.6	1.0	1.0	0.8	0.8	0.8	0.6	0.8	0.8	1.0
95th Percentile	1.2	1.4	1.6	1.6	1.4	1.8	1.2	2.0	2.1	1.6	2.2	1.6	1.0	2.0	1.6	1.4	2.6	2.4	1.4	2.2	1.6	1.4	1.8	2.4

Global Average

Layer#	Hoop Layer [Hp]	Middle Helical Layer [H1]	Base Helical Layer [H2]
Average	0.79	0.92	0.89
Std. Dev.	0.31	0.56	0.56
COV*10^{-2}	0.39	0.61	0.63
Median	0.70	0.75	0.72
95th Percentile	1.35	1.95	1.89

Table 3 Statistical data for variation semi-minor axis of ellipsoidal voids [mm × 10]

Intra-Laminate Average (S1 to S8)

Specimen#	Specimen 1			Specimen 2			Specimen 3			Specimen 4			Specimen 5			Specimen 6			Specimen 7			Specimen 8		
Layer	Hp	H1	H2	Hp	H1	H2	Hp	H1	H2	Hp	H1	H2	Hp	H1	H2	Hp	H1	H2	Hp	H1	H2	Hp	H1	H2
Average	0.43	0.45	0.47	0.52	0.45	0.47	0.48	0.64	0.51	0.44	0.71	0.46	0.41	0.59	0.46	0.64	0.78	0.58	0.55	0.61	0.45	0.57	0.68	0.69
Std. Dev.	0.18	0.18	0.22	0.28	0.19	0.28	0.21	0.38	0.21	0.17	0.45	0.17	0.11	0.41	0.24	0.24	0.51	0.34	0.18	0.39	0.20	0.18	0.44	0.46
COV*10^{-2}	0.41	0.41	0.48	0.54	0.42	0.49	0.39	0.59	0.42	0.39	0.65	0.38	0.25	0.68	0.53	0.37	0.64	0.59	0.32	0.64	0.45	0.32	0.64	0.67
Median	0.4	0.4	0.4	0.4	0.4	0.4	0.4	0.6	0.4	0.4	0.6	0.4	0.4	0.4	0.4	0.6	0.6	0.4	0.6	0.4	0.4	0.6	0.6	0.4
95th Percentile	0.8	0.8	0.8	0.8	0.8	1.2	1.0	1.4	1.0	0.8	1.6	0.8	0.6	1.4	1.1	1.0	1.8	1.2	0.9	1.4	0.8	1.0	1.4	1.8

Global Average

| Layer#	Hoop Layer [Hp]	Middle Helical Layer [H1]	Base Helical Layer [H2]
Average	0.51	0.61	0.51
Std. Dev.	0.19	0.37	0.26
COV*10^{-2}	0.38	0.58	0.50
Median	0.47	0.50	0.40
95th Percentile	0.92	1.32	1.03
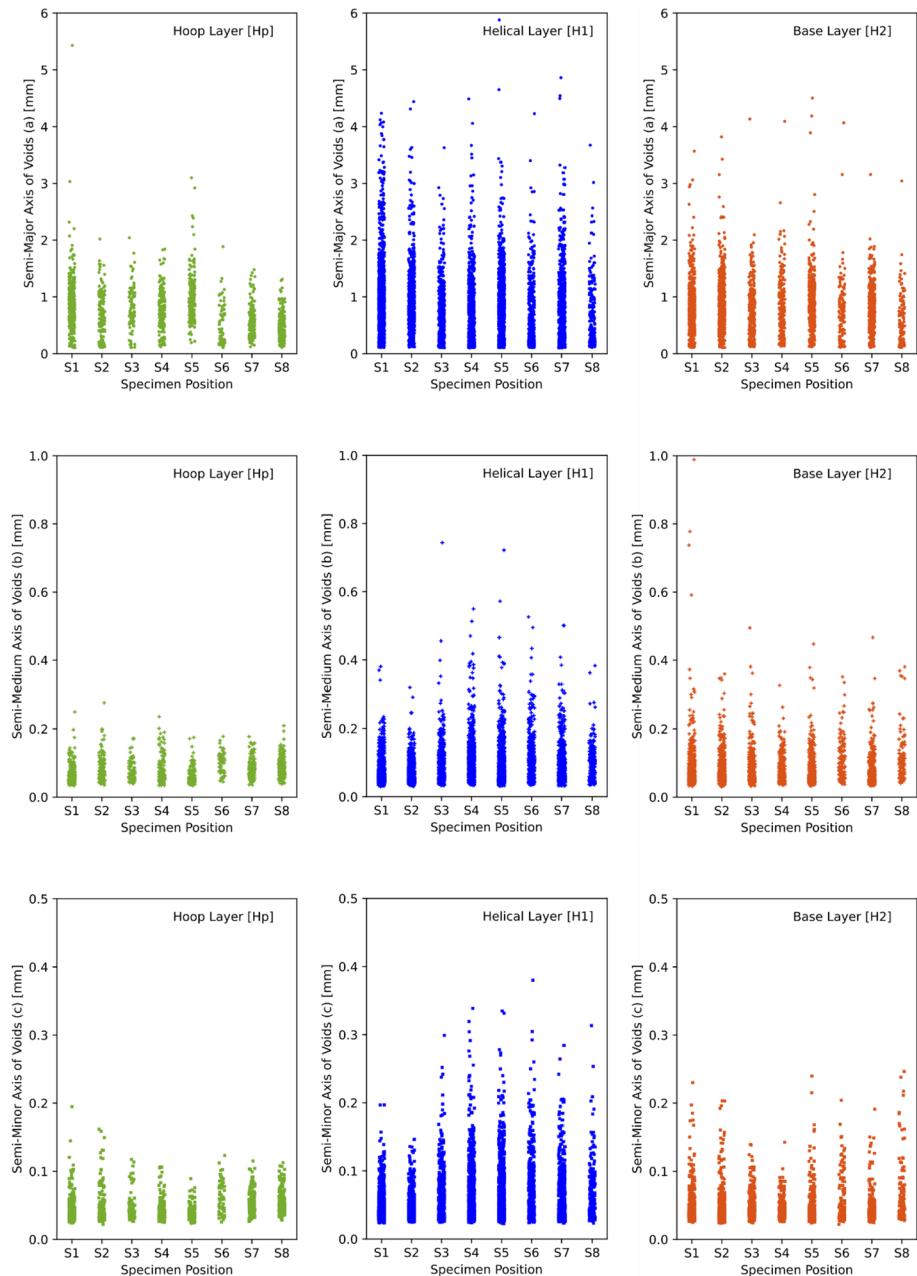
Fig. 9 Representation of the three size parameters viz: semi-major, semi-medium and semi-minor axes of the ellipsoids fitted to the PCA deviation data of the voids

helical layer interestingly increases from S1 to the centre (S4-S5) of the composite panel and again reduces towards the S8, with little to no change in the major axes length. This signifies that the voids in the middle are thicker or tend to be more circular. A comparison between

two different helical layers is also performed to assess the presence of changes based on the orientation difference. The average and the standard deviation for voids within the base helical layer [H2], amongst the semi-major, semi-medium and semi-minor axis of the voids, are 0.795 ± 0.50 mm, 0.089 ± 0.05 mm and 0.051 ± 0.02 mm, respectively. The base helical layers depict a similar distribution in size parameters compared to the hoop layer for composite specimens (S1 to S8). The scatter in the distribution is more pronounced, which is visible from a longer interquartile range of the size parameters. This scatter has a much higher interquartile range compared to the hoop layer. It can again be postulated that the voids are ellipsoids and have rather elliptical cross-sections, which are flatter due to a higher semi-medium and semi-minor axis ratio.

3.2 Analysis of Voids Morphology

3.2.1 Volume and Sphericity Correlation

The morphology and sphericity of each void can be calculated using the ellipsoidal fitted data. As the layers have been discretized using ROI analysis, the distribution can be presented based on the location of the voids. The volume of the individual void was calculated directly from the number and size of voxels that encompass each void directly from the micro-CT data. The ellipsoidal fitted volume was not selected. It can be noted that voids and delamination are differentiated by specifying a volume range of 0.01-6 mm^3 and sphericity above 0.15, thus filtering out delaminations, which can be wrongly interpreted as porosity within the filament-winded composite structures. It can be stated that the delaminations are usually long flat inter-laminar cracks and are present between the helical and hoop laminates, whereas voids are mostly closed spherical or elliptical objects and hence can be filtered out using above filter as also suggested by Mehdikhani et al. [36] The statistical data for the distribution of void volume and corresponding sphericity in individual layers is presented in Tables 4 and 5. In general terms, the void morphology in the dataset comprises two major types of voids: elongated, rod and blade type, and spherical pores/voids. The sphericity values range between 0 and 1, where the value tends to 1 is more compact and spherical. The smaller elongated pores are mostly intra-filament positioned inside the filament tape, a combination of glass fiber tape. The larger pores are placed between consecutive filaments and addressed as inter-filament voids. In addition to the elongated pores, spherical pores with sphericity close to 0.8 have been found to be located within the resin-rich areas of the composite coupon that favor their presence, as seen in Fig. 3 for the case of the helically winded layers of S1.

To understand the volumetric fraction based on the voids' morphology, the individual void's sphericity is compared with its volume for each laminate layer and each coupon (S1 to S8) along the winding direction. Several large values corresponding to a higher volume of voids have been removed to enhance the visualisation and interpretation of the diagram. Figure 10 presents the volume-sphericity distribution of voids in the hoop layer. The vertical line denotes the geometrical mean based on the sphericity. It can be observed that voids located inside the hoop layer have a relatively lower number and volume. Ellipsoidal voids where the mean sphericity is less than 0.4 are observed. Moving towards the winding direction, the geometrical sphericity mean increases, which implies the increased presence of rounder voids, which have a shorter major axis, as also observed in Fig. 9(a).

Table 4 Statistical data for variation in the volume of voids [mm^3 × 100]

Intra-Laminate Average (S1 to S8)

Specimen#	Specimen 1			Specimen 2			Specimen 3			Specimen 4			Specimen 5			Specimen 6			Specimen 7			Specimen 8		
Layer	Hp	H1	H2	Hp	H1	H2	Hp	H1	H2	Hp	H1	H2	Hp	H1	H2	Hp	H1	H2	Hp	H1	H2	Hp	H1	H2
Average	1.38	1.66	2.23	1.36	1.49	1.81	1.34	2.14	1.67	1.30	1.30	1.38	1.26	2.16	3.17	1.63	2.52	1.61	1.44	1.96	1.03	1.30	1.91	2.14
Std. Dev.	1.85	2.72	14.42	1.23	1.98	4.46	0.94	6.84	3.15	0.95	0.95	1.26	0.96	6.95	19.75	1.36	4.91	2.03	1.13	2.88	1.30	0.87	4.27	3.34
COV*10^{-4}	1.63	1.87	7.29	1.09	1.54	2.81	0.78	3.49	2.12	0.84	0.84	1.13	0.90	3.54	6.77	0.92	2.06	1.43	0.78	1.61	1.26	0.74	2.44	1.81
Median	0.68	0.73	0.65	0.70	0.77	0.74	0.79	0.81	0.74	0.79	0.79	0.71	0.73	0.80	0.67	0.91	0.96	0.75	0.99	0.92	0.68	0.82	0.84	0.73
95th Percentile	2.65	4.40	2.65	3.44	3.71	3.24	2.92	5.34	3.65	2.77	2.77	3.15	2.98	4.99	3.15	3.70	8.67	4.65	4.01	6.09	2.27	2.91	4.52	6.09

Global Average

Layer#	Hoop Layer [Hp]	Middle Helical Layer [H1]	Base Helical Layer [H2]
Average	1.37	2.02	1.87
Std. Dev.	1.16	4.54	6.21
COV*10^{-4}	0.96	2.41	3.08
Median	0.78	0.83	0.70
95th Percentile	3.17	5.55	3.61

Table 5 Statistical data for variation in sphericity of voids [--]

Intra-Laminate Average (S1 to S8)

Specimen#	Specimen 1			Specimen 2			Specimen 3			Specimen 4			Specimen 5			Specimen 6			Specimen 7			Specimen 8		
Layer	Hp	H1	H2	Hp	H1	H2	Hp	H1	H2	Hp	H1	H2	Hp	H1	H2	Hp	H1	H2	Hp	H1	H2	Hp	H1	H2
Average	0.31	0.29	0.31	0.34	0.30	0.31	0.32	0.37	0.33	0.33	0.37	0.32	0.28	0.36	0.31	0.36	0.40	0.34	0.39	0.37	0.31	0.41	0.36	0.34
Std. Dev.	0.08	0.08	0.09	0.12	0.09	0.08	0.10	0.14	0.10	0.10	0.15	0.09	0.04	0.14	0.09	0.10	0.15	0.13	0.08	0.14	0.08	0.09	0.14	0.12
COV*10^{-2}	0.27	0.27	0.29	0.35	0.31	0.26	0.31	0.38	0.31	0.31	0.39	0.31	0.16	0.41	0.29	0.28	0.38	0.38	0.21	0.40	0.26	0.23	0.37	0.36
Median	0.29	0.28	0.28	0.30	0.27	0.29	0.30	0.31	0.29	0.30	0.32	0.28	0.28	0.29	0.28	0.33	0.34	0.28	0.38	0.29	0.29	0.41	0.31	0.29
95th Percentile	0.51	0.48	0.56	0.63	0.54	0.51	0.58	0.63	0.57	0.55	0.64	0.55	0.35	0.64	0.55	0.53	0.63	0.61	0.53	0.63	0.49	0.56	0.62	0.61

Global Average

Layer#	Hoop Layer [Hp]	Middle Helical Layer [H1]	Base Helical Layer [H2]
Average	0.34	0.35	0.32
Std. Dev.	0.09	0.13	0.11
COV*10^{-2}	0.26	0.36	0.31
Median	0.32	0.30	0.28
95th Percentile	0.53	0.61	0.55
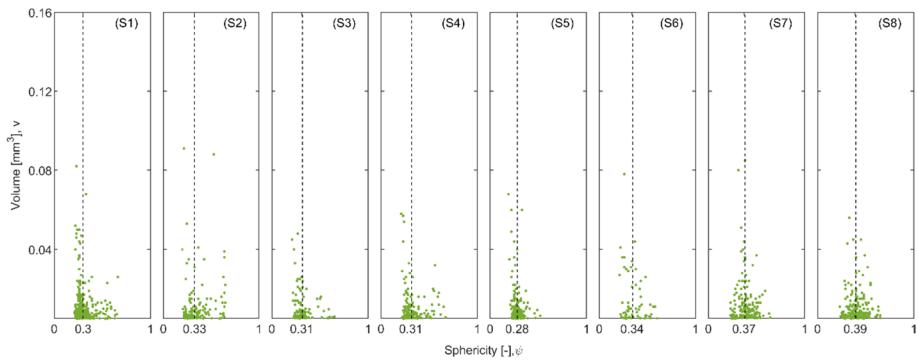
Fig. 10 Sphericity versus volume of voids in the hoop layer [Hp] inside composite coupons (S1 to S8)

In the case of the middle helical layer [H1] as presented in Fig. 11, two major types of voids are detected. More specifically, specimens S1, S2 and, S7, S8, which are taken from the top and the bottom of the axial panel, respectively, favour the presence of long elliptical voids, but following the winding direction, spherical voids seen to appear with the highest volume fraction observed for specimens taken from the centre of the panel. The highest interquartile variation of the volume and the sphericity is also observed for this layer. It can be observed that the porosity content in the middle helical layers is generally higher compared to the base and hoop-winded layers, as also presented in Fig. 12. The observation is also consistent with the work of Rojek et al. [46], in which similar porosity morphology was observed, leading to the conclusion that the helical layers have higher void content. This higher content can be explained by the lower compaction the helical layers receive and the lower winding tension applied during the fabrication process, as explained in the earlier work of Cohen [47]. Thus, after the solidification and curing of the matrix, the middle layers often exhibit voids entrapped within the polymeric matrix and possess a spherical cross-section, as reported by references [27, 34, 36, 39, 40].

Figure 12 presents the correlation between the volume and sphericity for voids detected in the base helical layer. It is again observed that the laminate favours the presence of long
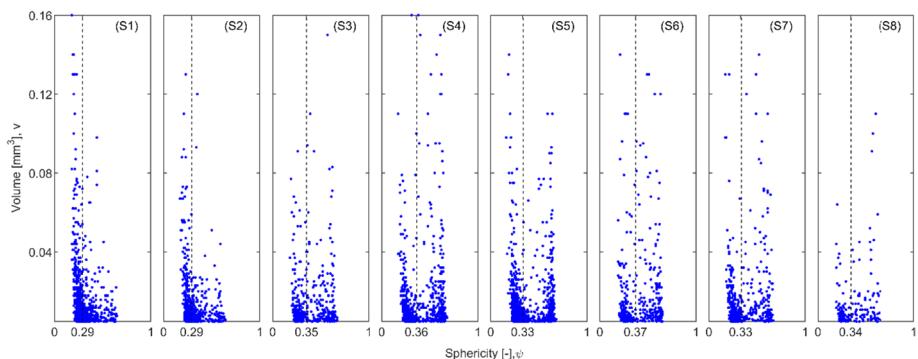
Fig. 11 Variation of sphericity versus volume of voids in the middle helical layer [H1] of composite coupons (S1 to S8)
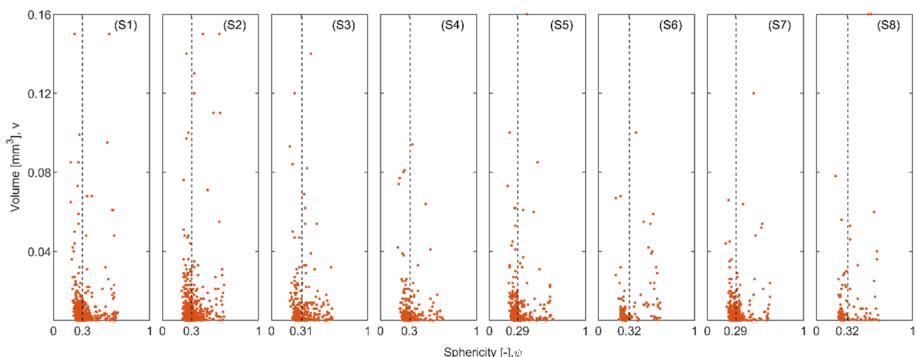
Fig. 12 Variation of sphericity versus volume of voids in the bottom helical layer [H2] of composite coupons (S1 to S8)

elliptical voids, with an average sphericity of 0.3. The number of voids detected also seems to decrease towards the winding direction. The observations are similar to the circumferential hoop layer. It can be hypothesised that the winding angle creates voids with different sphericity and volumes. It is observed that when the winding is circumferential or low angle ($\pm15°$) like the base layer, the compaction is adequate to squeeze the matrix out and thus leading to a small number of spherical voids and larger elliptical voids, which are primarily present between the tows of the filament. On the other hand, a high angle (±75) seems to favour more matrix-trapped spherical voids.

Nevertheless, between different coupons, even though the voids fall in a distribution, the overall volumetric porosity and number of voids are not the same for all specimens. To resolve the sigmoidal trend in the overall porosity volume fraction presented in Fig. 7, the directional variability along the filament winding direction from S1 to S8 was carried out for each layer and is termed as "smeared porosity". To calculate the average smeared porosity, each coupon was segmented into slices separated by 0.5 mm. The porosity values was measured in each slice along the winding direction. The average porosity in each slice was measured as fraction of the grey intensity value corresponding to voids and bulk of the material, as also defined in [48]. The average smeared porosity over each sample S1 to S8 along the winding direction is presented in Fig. 13. The volumetric porosity (%) and the number of voids detected in each individual sample with a defined grey scale intensity threshold are presented in Table 6. It can be postulated that for both the hoop layer and middle helical layer [H1], the trend is again sigmoidal with a much less volumetric fraction of porosity in the hoop layer. An upsurge of increased porosity is observed towards the centre of the axial panel in the base layer [H2], where large flat and long elongated voids are visible in Fig. 6(S1) and (S5), respectively. This was attributed to a series of gaps between filaments, which can be created during the winding process towards the edge and centre of the panel. During the winding process, the gaps are encapsulated within the polymer matrix during the lamination process, creating large voids that are also well aligned along the filament winding direction. Similar observations have also been reported by Stamopoulos et al. [49]. In addition, even though, in general terms, the porosity content is expected to increase while moving from base helical to circumferential hoop winding layers, the variation of the winding angle (from base layer to middle helical and then hoop) can lead to different results.
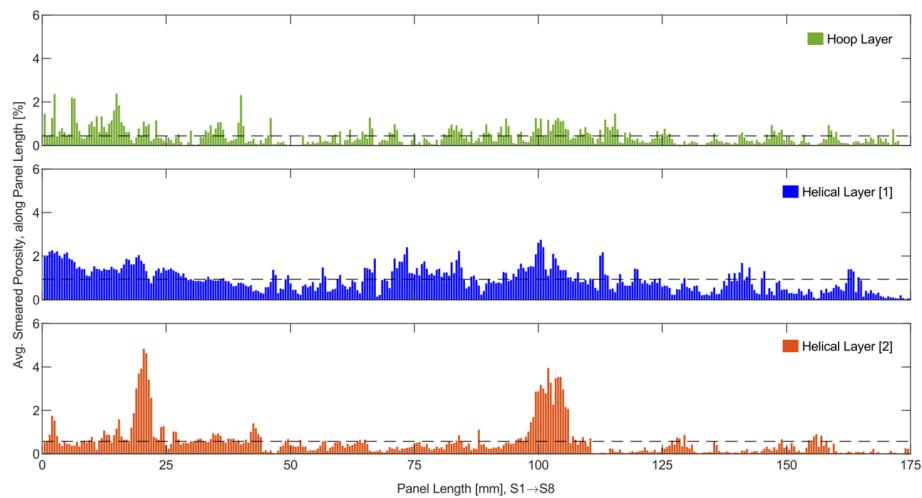
Fig. 13 Directional variability of porosity inside the composite panel along the filament winding direction

3.2.2 Shape Analysis

Characterizing the form of voids' three-dimensional shape is performed by calculating the voids' flatness and elongation and plotting them on a Zingg diagram [44]. The flatness (fl) is the measure of how flaky or platy the void' is, while the elongation (el) is the measure of the void's rod-like shape. By plotting the Zingg elongation and flatness parameter, the void morphology can be categorized into four classes: (I) oblate (disk/plate-like), (II) compact, (III) blade-like and (IV) prolate (rod) where the partition lines are drawn at el = 2/3 and fl = 2/3 as presented in Fig. 14(b). Isolines are plotted as intercept sphericity values, which help in the classification of morphology [50].

Table 6 Number of voids (n) detected and void volume fraction (V_v) inside specimens along the filament winding direction

Specimen Label	Hoop Layer (Hp)		Middle Helical Layer (H1)		Base Helical Layer 2 (H2)	
	Voids [%]	n	Voids [%]	n	Voids [%]	n
S1	1.04	355	1.81	1321	1.28	639
S2	0.45	148	0.94	779	0.71	633
S3	0.26	95	0.76	464	0.35	311
S4	0.36	155	1.34	805	0.34	220
S5	0.64	212	1.33	1099	1.35	442
S6	0.40	142	0.81	422	0.21	135
S7	0.28	163	0.62	280	0.17	128
S8	0.24	178	0.39	198	0.19	118
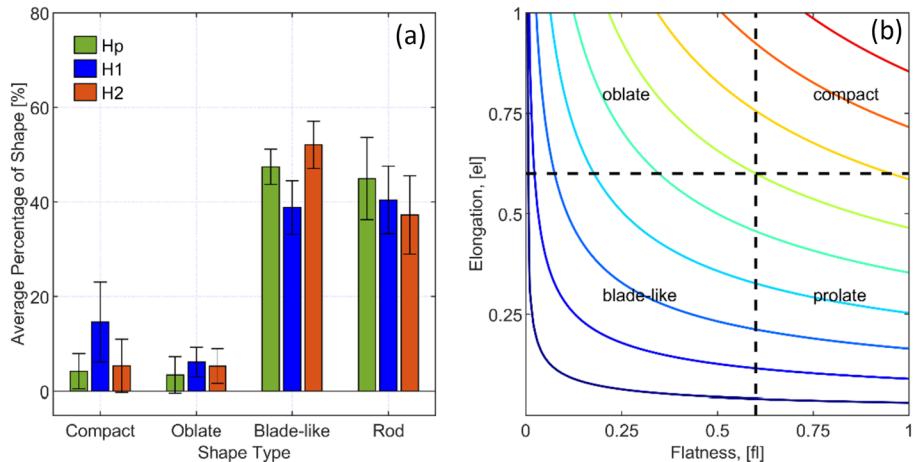
Fig. 14 a Average shape distribution percentage of voids inside hoop and helical layers **b** Zingg Plot

Figure 15, presents the variation of Zingg parameters (el and fl) for voids detected inside each composite coupon S1 to S8 for circumferential hoop layer. It can be observed that the majority of the voids are prolate and thus have rod-like and blade-like shapes. The specimens taken from the bottom of the panel (S7, S8) interestingly have an increase towards compacted voids, which are still rod-like but possess a relatively shorter semi-major axis.

Figures 16 and 17 present the variation of void morphologies inherently to each of the specimens S1 to S8 for helical layers. For the helical layer, specifically the middle layer [H1], it can be noted that voids are still elongated in shape, but many of them fall in the compact region of the Zingg plot. This was attributed to many spherical voids inside the matrix rather than within the tows. The highest-frequency spherical voids are visible in the middle of the panel. Figure 14(a) presents the percentage distribution of void shape, where it can be observed that the blade-like thin voids and rod-shaped voids are more prevalent overall, but compact spherical voids are primarily present within middle helical layers [H1].
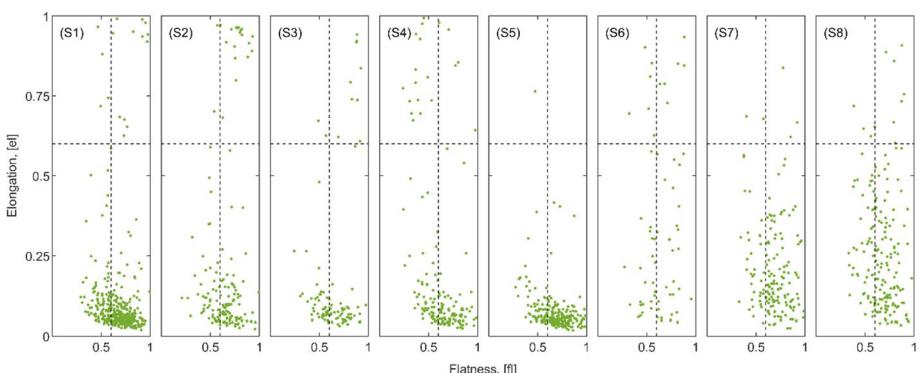
Fig. 15 Elongation vs flatness Zingg plot for identification of void morphology in hoop layers of composite coupons (S1 to S8)
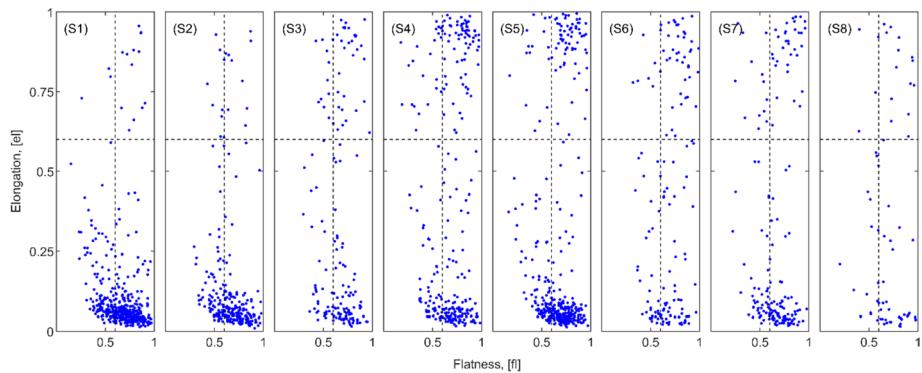
**Fig. 16** Elongation vs flatness Zingg plot for identification of void morphology in helical layers [1] of composite coupons (S1 to S8)

3.3 Fiber and void orientation analysis

The mean plane projected orientation of the voids in each laminate layer was compared with the mean fiber orientations to estimate the degree of misorientations within the filament-winded composite panel. The mean value is taken over samples from S1 to S8 along the filament winding direction. The plane projected orientation angle is calculated as the angle between PCA1, which is the principal axes of the voids or the fiber and the reference axis on the plane on which the 3D orientations are being projected. The orientations hence vary between a value of 0° to 180°. The frequency distribution curves for the plane projected orientations are presented in Fig. 18.

It can be mentioned that generally, the voids in the hoop and helical layers are aligned along the nominal fiber direction and the relative intensity and frequency of the voids are comparatively lower, which can be correlated to a lower number of voids compared to each
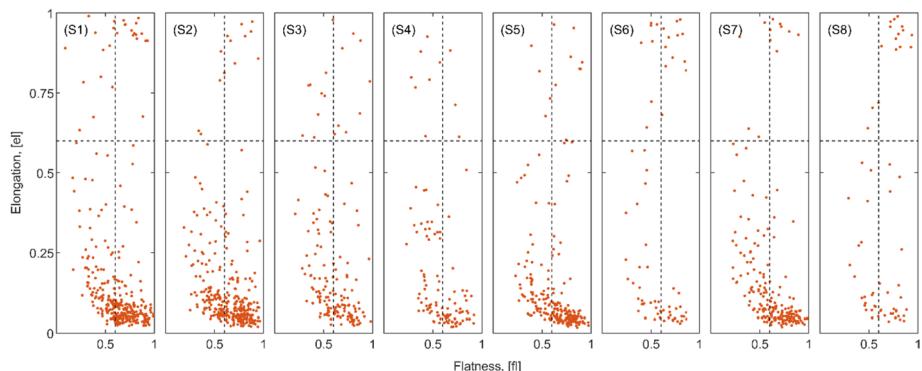
Fig. 17 Elongation vs flatness Zingg plot for identification of void morphology in helical layers [2] of composite coupons (S1 to S8)
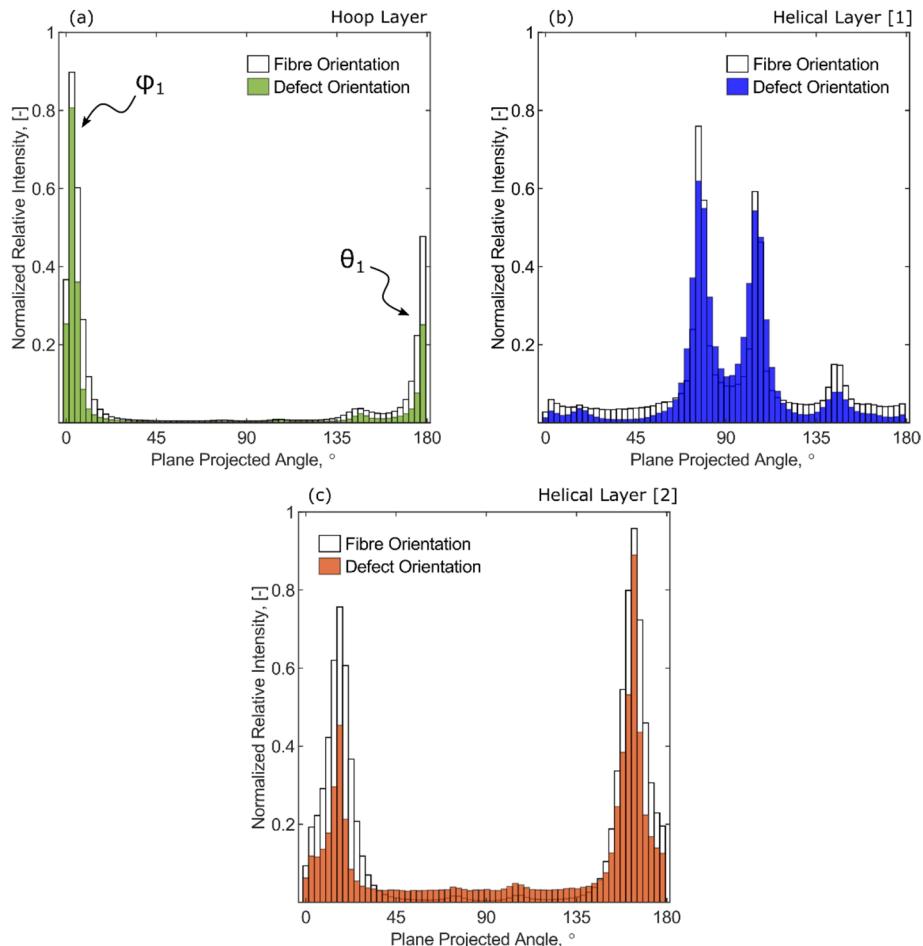
Fig. 18 Frequency distribution plot for the variation of plane projected orientation of fibers and voids located within the tows and polymeric matrix

individual fiber. Table 7 presents the mean-plane projected angles for the voids and fiber along the 2 major orientations (φ,θ) with the corresponding standard deviation. When comparing the average individual layer orientations, it can be observed that the hoop layer has a higher degree of deviation in fiber and voids orientations when compared to helical layers. This can be attributed to a final tow overwrapped at an angle to finish the winding process and increase compaction. These orientations are visible in Fig. 4(e, f). The mean misorientations are calculated individually as the difference between the nominal fiber and void orientations along the major directions. The degree of the misalignment is found to be relatively low, while the highest value is observed for the base layer, which is wrapped helically [H2].

Table 7 Plane projected orientation data for voids and fiber detected in hoop layers and helical layers of samples from S1 to S8

Laminate	Mean 1st Major Orientation, Fiber (φ_f)	Standard deviation ($\sigma_{\varphi f}$)	Mean 1st Major Orientation, Defect (φ_d)	Standard deviation ($\sigma_{\varphi d}$)	Mean 2nd Major Orientation, Fiber (θ_f)	Standard deviation ($\sigma_{\theta f}$)	Mean 2nd Major Orientation, Defect (θ_d)	Standard deviation ($\sigma_{\theta d}$)	Misorientation ($\varphi_f - \varphi_d$)	Misorientation ($\theta_f - \theta_d$)
Hoop Layers [Hp]	2.55	1.40	2.46	1.41	178.51	0.97	178.22	1.25	0.08	0.29
Middle Helical Layer-1 [H1]	77.11	0.82	77.29	1.12	105.17	0.92	105.52	0.75	-0.17	-0.35
Base Helical Layer-2 [H2]	16.84	1.09	16.93	0.98	163.23	0.72	161.91	2.66	-0.08	1.32

4 Conclusion and Summary

A comprehensive 3D analysis of voids and fiber in an as-manufactured representative unit panel from a glass fiber/vinyl ester filament winded composite structure has been presented using X-ray computed tomography. The voids identified are representative of the voids that can be found in a typical filament-winded structure. A curved cylindrical panel of a filament-winded structure was extracted along the axial direction and was used to study the variation in the size and volume of the voids along its tubular length and filament-winding direction. The fiber, matrix and voids were segmented using a standardised greyscale segmentation process. Statistical data are presented for void characteristics.

- It can be observed that the majority of the voids detected inside are elongated with a varying cross-section, depending on the location, with an average sphericity of 0.34. Spherical voids are observed in the composite layers with resin-rich areas and often present with average sphericity greater than 0.5 and relatively higher volume when compared to long elliptical voids. It has been observed that the major axis of the voids follows the tow orientation during the filament winding.
- The highest misorientation is approximately 1.32° observed for the base helical layer. This could be attributed to a weaker tension during winding.
- It is also observed that the overall volume fraction of the voids follows a sinusoidal transition, with the highest porosity in specimens S4 and S5, which are located towards the centre of the axial panel. The highest average voidage reported is approximately 1.35% for the middle helical layer.
- When individual layers are examined, moving through the thickness of the composite coupon viz. circumferential hoop layer [Hp], middle helical layer [H1] and base helical layer [H2], it can be observed that the highest number of voids are detected for the middle layer, followed by the base and the top circumferential hoop layer. The middle layer also hosts the highest average porosity volume fraction, with many spherical voids trapped in the vinyl ester matrix. Hence, the position of voids is dependent on the winding sequence.

In summary, this study successfully employed micro-CT imaging, ROI analysis and discretising porosity inside a laminated filament winded composite structure based on the location and winding direction. The data extracted was used to study pore characteristics like the volume of each pore, shape, size and orientation. The results can be utilised in studying matrix-dominated failures through numerical and finite element methods, which accommodate the effect of void orientations and volumetric content. To valorise the results from this study, one has to include the effect of geometry, orientation, and size of the specimen for the composite laminate system in the study, as the voids presented here are primarily macro-voids, where the micro-voids are assumed to be causing an insignificant effect on the mechanical properties. In addition, the findings may be considered as a step forward to a further development of protocols that contribute to the amelioration of the quality of the manufacturing process, testing coupon selection and the overall product as well. In conclusion, the outcome of this study could be a useful tool to aggregate porosity through a novel graphical technique called "MObject" [33] and study failure via knockdown factors used for the calculation of strength degradation as a function of void volume fraction.

Data Availability The data that support the findings of this study are available from the corresponding author upon reasonable request.

Declarations

Conflicts of Interest The author declares no conflict of interest and its an original work.

References

1. Mottram, J.T., et al.: Design of fibre-polymer composite structures–European Technical Specification: Combined stresses. In: 20th European Conference on Composite Materials: Composites Meet Sustainability. EPFL Lausanne, Composite Construction Laboratory (2022)
2. Peters, S., Tarnopol'skii, Y.M.: Filament winding. In: Composites Engineering Handbook, pp. 527–560. CRC Press (1997)
3. Azeem, M., et al.: Application of filament winding technology in composite pressure vessels and challenges: a review. J. Energy Storage **49**, 103468 (2022)
4. Kong, C., S. Lim, H. Park.: A study on optimal design of filament winding composite tower for 2 MW class horizontal axis wind turbine systems. in Turbo Expo: Power for Land, Sea, and Air. American Society of Mechanical Engineers (2013)
5. Bodea, S., et al.: Robotic coreless filament winding for hyperboloid tubular composite components in construction. Autom. Constr. **126**, (2021)
6. Shen, F.C.: A filament-wound structure technology overview. Mater. Chem. Phys. **42**(2), 96–100 (1995)
7. Zweifel, P., S.F. Fennessey.: Thermal conductivity of reinforced composites for electrical applications. In: 2010 IEEE International Symposium on Electrical Insulation. IEEE (2010)
8. Toso, Y.M.P.: Effective automated tape winding process with on-line bonding under transient thermal conditions. ETH Zurich (2003)
9. Peters, S.T.: Composite filament winding. ASM International (2011)
10. Betts, D., Sadeghian, P., Fam, A.: Experimental and analytical investigations of the flexural behavior of hollow±55° filament wound GFRP tubes. Thin-Walled Struct. **159**, 107246 (2021)
11. Colombo, C., Vergani, L.: Optimization of filament winding parameters for the design of a composite pipe. Compos. B. Eng. **148**, 207–216 (2018)
12. Lisbôa, T.V., et al.: FEM updating for damage modeling of composite cylinders under radial compression considering the winding pattern. Thin-Walled Struct. **173**, 108954 (2022)
13. Dalibor, I., et al.: A geometric approach for filament winding pattern generation and study of the influence of the slippage coefficient. J. Braz. Soc. Mech. Sci. Eng. **41**(12), 1–16 (2019)

14. Rousseau, J., Perreux, D., Verdiere, N.: The influence of winding patterns on the damage behaviour of filament-wound pipes. Compos. Sci. Technol. **59**(9), 1439–1449 (1999)
15. de Almeida, S.F.M., Neto, Z.D.S.N.: Effect of void content on the strength of composite laminates. Compos. Struct. **28**(2), 139–148 (1994)
16. Sisodia, S., et al.: Effects of voids on quasi-static and tension fatigue behaviour of carbon-fibre composite laminates. J. Compos. Mater. **49**(17), 2137–2148 (2015)
17. Stamopoulos, A., Tserpes, K., Dentsoras, A.: Quality assessment of porous CFRP specimens using x-ray computed tomography data and artificial neural networks. Compos. Struct. **192**, 327–335 (2018)
18. Campbell, F.C., Mallow, A.R., Browning, C.E.: Porosity in carbon fiber composites an overview of causes. J. Adv. Mater. **26**(4), 18–33 (1995)
19. Lamontia, M.A., et al.: Manufacturing flat and cylindrical laminates and built up structure using automated thermoplastic tape laying, fiber placement, and filament winding. SAMPE J. **39**(2), 30–43 (2003)
20. Ren, M., et al.: Study of one-dimensional cure simulation applicable conditions for thick laminates and its comparison with three-dimensional simulation. Sci. Eng. Compos. Mater. **25**(6), 1197–1204 (2018)
21. Ledru, Y., et al.: Coupled visco-mechanical and diffusion void growth modelling during composite curing. Compos. Sci. Technol. **70**(15), 2139–2145 (2010)
22. Lehman, M.: Void formation and transport during composite laminate processing: an initial model framework. Composite Materials: Quality Assurance and Processing, p. 96. (1983)
23. Loos, A.C., Springer, G.S.: Curing of epoxy matrix composites. J. Compos. Mater. **17**(2), 135–169 (1983)
24. Li, M., et al.: A simple method for the measurement of compaction and corresponding transverse permeability of composite prepregs. Polym. Compos. **28**(1), 61–70 (2007)
25. Shin, D.D., Hahn, H.T.: Compaction of thick composites: simulation and experiment. Polym. Compos. **25**(1), 49–59 (2004)
26. Stedile Filho, P., Almeida, J.H.S., Jr., Amico, S.C.: Amico: Carbon/epoxy filament wound composite drive shafts under torsion and compression. J. Compos. Mater. **52**(8), 1103–1111 (2018)
27. Chen, R.K., et al.: Nano-CT characterization of structural voids and air bubbles in fused deposition modeling for additive manufacturing. in International Manufacturing Science and Engineering Conference. American Society of Mechanical Engineers (2015)
28. Dierick, M., et al.: The use of 2D pixel detectors in micro-and nano-CT applications. Nucl. Instrum. Methods Phys. Res., Sect. A **591**(1), 255–259 (2008)
29. Saucedo-Mora, L., et al.: In situ observation of mechanical damage within a SiC-SiC ceramic matrix composite. J. Nucl. Mater. **481**, 13–23 (2016)
30. Mizutani, R., Suzuki, Y.: X-ray microtomography in biology. Micron. **43**(2–3), 104–115 (2012)
31. Tjong, W., et al.: The effect of voxel size on high-resolution peripheral computed tomography measurements of trabecular and cortical bone microstructure. Med. Phys. **39**(4), 1893–1903 (2012)
32. Pareyt, B., et al.: The role of sugar and fat in sugar-snap cookies: Structural and textural properties. J. Food Eng. **90**(3), 400–408 (2009)
33. Tserpes, K., Stamopoulos, A., Pantelakis, S.G.: A numerical methodology for simulating the mechanical behavior of CFRP laminates containing pores using X-ray computed tomography data. Compos. Part B Eng. **102**, 122–133 (2016)
34. Mehdikhani, M., et al.: Voids in fiber-reinforced polymer composites: A review on their formation, characteristics, and effects on mechanical performance. J. Compos. Mater. **53**(12), 1579–1669 (2019)
35. Bossi, R.H., K.K. Cooprider, G.E. Georgeson: X-ray computed tomography of composites. Boeing Aerospace and Electronics Co Seattle Wa (1990)
36. Mehdikhani, M., et al.: Detailed characterization of voids in multidirectional carbon fiber/epoxy composite laminates using X-ray micro-computed tomography. Compos. Part A: Appl. Sci. Manufac. **125**, (2019)
37. Pyka, G., et al.: The effect of spatial micro-CT image resolution and surface complexity on the morphological 3D analysis of open porous structures. Mater. Charact. **87**, 104–115 (2014)
38. Sisodia, S.M., et al.: High-resolution computed tomography in resin infused woven carbon fibre composites with voids. Compos. Sci. Technol. **131**, 12–21 (2016)
39. Little, J.E., Yuan, X., Jones, M.I.: Characterisation of voids in fibre reinforced composite materials. NDT & E Int. **46**, 122–127 (2012)
40. Nikishkov, Y., Airoldi, L., Makeev, A.: Measurement of voids in composites by X-ray Computed Tomography. Compos. Sci. Technol. **89**, 89–97 (2013)
41. Stamopoulos, A., et al.: Evaluation of porosity effects on the mechanical properties of carbon fiber-reinforced plastic unidirectional laminates by X-ray computed tomography and mechanical testing. J. Compos. Mater. **50**(15), 2087–2098 (2016)
42. Plank, B., G. Rao, J. Kastner.: Evaluation of CFRP-reference samples for porosity made by drilling and comparison with industrial porosity samples by means of quantitative X-ray computed tomography. In: 7th International Symposium on NDT in Aerospace (2015)

43. Tretiak, I., Smith, R.A.: A parametric study of segmentation thresholds for X-ray CT porosity characterisation in composite materials. Compos. Part A: Appl. Sci. Manufac. **123**, 10–24 (2019)
44. Zingg, T.: Beitrag zur schotteranalyse. ETH Zurich (1935)
45. Padfield, D., Miller, J.: A label geometry image filter for multiple object measurement. Insight J. **301**, 1–13 (2008)
46. Rojek, J., et al.: Modelling the effect of porosity on the mechanical properties of unidirectional composites. The case of thick-walled pressure vessels. In: ECCM 18-18th European Conference on Composite Materials (2018)
47. Cohen, D.: Influence of filament winding parameters on composite vessel quality and strength. Compos. Part A: Appl. Sci. Manufac. **28**(12), 1035–1047 (1997)
48. Morales-Rodriguez, A., et al.: Porosity analysis of long-fiber-reinforced ceramic matrix composites using X-ray tomography. Scripta Mater. **60**(6), 388–390 (2009)
49. Stamopoulos, A., et al.: Identification of the characteristics of helicoidally filament wound tubes using vision systems. Procedia Comput. Sci. **217**, 1048–1056 (2023)
50. Orosz, Á, Angelidakis, V., Bagi, K.: Surface orientation tensor to predict preferred contact orientation and characterise the form of individual particles. Powder Technol. **394**, 312–325 (2021)